

M²BeamLLM: Multimodal Sensing-empowered mmWave Beam Prediction with Large Language Models

Can Zheng, Jiguang He, *Senior Member, IEEE*, Chung G. Kang, *Senior Member, IEEE*, Guofa Cai, *Senior Member, IEEE*, Zitong Yu, *Senior Member, IEEE*, Mérouane Debbah, *Fellow, IEEE*

Abstract—This paper introduces a novel neural network framework called M²BeamLLM for beam prediction in millimeter-wave (mmWave) massive multi-input multi-output (mMIMO) communication systems. M²BeamLLM integrates multi-modal sensor data, including images, radar, LiDAR, and GPS, leveraging the powerful reasoning capabilities of large language models (LLMs) such as GPT-2 for beam prediction. By combining sensing data encoding, multimodal alignment and fusion, and supervised fine-tuning (SFT), M²BeamLLM achieves significantly higher beam prediction accuracy and robustness, demonstrably outperforming traditional deep learning (DL) models in both standard and few-shot scenarios. Furthermore, its prediction performance consistently improves with increased diversity in sensing modalities. Our study provides an efficient and intelligent beam prediction solution for vehicle-to-infrastructure (V2I) mmWave communication systems.

Index Terms—Beam prediction, massive multi-input multi-output (mMIMO), large language models (LLMs), multimodal.

I. INTRODUCTION

Millimeter-wave (mmWave) frequency bands offer broader channel bandwidths compared to traditional sub-6 GHz bands, enabling higher capacity for communication systems. However, their high propagation loss introduces new challenges for system design. While high-gain narrow beams formed by large antenna arrays can effectively compensate for the high path loss, the resulting strong directional characteristics make the beams highly sensitive to user mobility and environmental obstructions [1]. This sensitivity can lead to a significant decline in the stability of mmWave connectivity. In this context, beam alignment (BA) becomes a crucial technology for determining the optimal/sub-optimal beamforming direction, playing a key role in establishing reliable communication links.

C. Zheng and C. G. Kang are with the Department of Electrical and Computer Engineering, Korea University, Seoul 02841, South Korea (e-mail: zc331_@korea.ac.kr, ccgkang@korea.ac.kr).

J. He and Z. Yu are with the School of Computing and Information Technology, Great Bay University, Dongguan Key Laboratory for Intelligence and Information Technology, and Great Bay Institute for Advanced Study (GBIAS), Dongguan 523000, China (e-mail: jiguang.he@gbu.edu.cn, zitong.yu@ieee.org).

G. Cai is with School of Information Engineering, Guangdong University of Technology, Guangzhou, China (e-mail: caiguoфа2006@gdut.edu.cn).

M. Debbah is with the Center for 6G Technology, Khalifa University of Science and Technology, Abu Dhabi, United Arab Emirates (e-mail: merouane.debbah@ku.ac.ae).

In vehicle-to-everything (V2X) scenarios, the high mobility of user equipment (UE) imposes even more stringent requirements on BA mechanisms. Compared to general mobile scenarios, the rapid topology changes unique to mmWave V2X significantly increase the complexity of real-time alignment for beams. Frequent beam misalignment can lead not only to communication link interruptions but also to severe degradation of communication quality. Existing BA solutions rely on repeated beam training processes to determine the optimal beam direction, but the resource-intensive nature of this process can encroach upon time slot resources allocated for data transmission, resulting in reduced system throughput. Therefore, developing intelligent BA mechanisms that offer efficiency and robustness has become a key research direction for ensuring the reliability of mmWave V2X communications.

The recent advancements in integrated sensing and communication (ISAC) have brought significant attention to sensing-empowered beam prediction. The optimal beam pair between the base station (BS) and UE is determined by their instantaneous spatial positions and the surrounding environment. Proactively utilizing UE positioning data alongside sensing data measured by the BS for beam prediction is a viable strategy to eliminate beam training overhead. Beam prediction based on historical sensing data essentially involves analyzing the complex interplay between the temporal dimension (historical state evolution) and the spatial dimension (environmental physical characteristics) of sensing data. This analysis is aimed at constructing mathematical models that reveal hidden dynamic patterns and establish a dynamic mapping between sensing data and future beam states. This task is particularly well-suited for deep learning (DL) methods, which can effectively capture and model such intricate relationships [2]. Prior studies have explored the use of various communication and sensing modalities—such as sub-6 GHz channel state information (CSI) [3], RGB images [4], radar [5], LiDAR [6], and GPS [7]—in conjunction with DL architectures for beam prediction.

The rapid development of large language models (LLMs), such as ChatGPT [8] and DeepSeek [9], introduces new possibilities for physical-layer applications that go beyond the limitations of conventional methods. LLMs, with their billions of parameters, exhibit exceptional capabilities in natural language understanding and logical reasoning. Owing to extensive pretraining on diverse and large-scale datasets, LLMs can achieve strong performance with minimal task-specific fine-

tuning. Compared to training transformer models from scratch, LLMs require significantly less labeled data, making them particularly advantageous in real-world applications where collecting and annotating large-scale supervised datasets is often impractical. Recent efforts have explored leveraging LLMs for physical-layer tasks, such as mmWave beam prediction. A representative example is BeamLLM [10], which utilizes LLMs to predict beam directions in vehicle-to-infrastructure (V2I) scenarios. While BeamLLM demonstrates strong prediction performance, its reliance on a single sensing modality—namely RGB images—limits its adaptability in complex and dynamic environments where visual information alone may be insufficient due to occlusions, lighting changes, or adverse weather conditions. To address this limitation, a more recent study [11] has attempted to integrate GPS positioning data and RGB images for multimodal beam prediction. This work highlights the potential of cross-modal fusion in enhancing robustness. However, it suffers from two limitations. First, it relies on large-scale GPT-4 models whose inference latency renders the approach unsuitable for real-time applications. For practical deployment, a more feasible solution would leverage historical data to predict future beam, aligning better with real-world requirements. Second, still only a limited number of modalities and lacking adaptability to environmental variations.

Beyond this, some prior works have investigated more generalized multimodal fusion frameworks to improve prediction robustness. For example, Shi *et al.* [12] explored combining multimodal sensing data, yet the fusion was static and based on naive concatenation. In contrast, Zhang *et al.* [13] introduced a more dynamic mixture-of-experts (MoE) framework, in which a gating network assigned weights to each modality. In addition, Cui *et al.* [14] established the relationship between different modalities through cross-attention.

In this paper, we introduce M²BeamLLM, a multimodal sensing empowered beam prediction framework built upon LLMs. Our major contributions are summarized as follows:

- 1) Our M²BeamLLM framework integrates multiple data sources—images, radar, LiDAR, and GPS. This multimodal approach enables a more comprehensive understanding of the environment, significantly enhancing the accuracy and robustness of beam prediction, particularly in dynamic scenarios.
- 2) We pioneer the application of LLMs, specifically GPT-2, to the beam prediction task, which has traditionally been addressed using DL architectures, e.g., recurrent neural networks (RNNs) [4]. By leveraging the superior generalization and reasoning capabilities of LLMs, we effectively model complex relationships within multimodal data, an approach that remains largely unexplored in existing studies.
- 3) Through supervised fine-tuning (SFT) of a pretrained LLM [15], we enable the model to adapt to the beam prediction task with minimal training data and computational cost. This contrasts sharply with the resource-intensive approaches of training models from scratch, offering a more efficient solution for practical deployment.
- 4) Experimental results demonstrate that M²BeamLLM

outperforms state-of-the-art DL models in both standard and few-shot prediction scenarios. Our framework achieves a Top-1 accuracy of 68.9%, surpassing the next-best method by 13.9%, and maintains superior performance even under challenging few-shot conditions.

- 5) Through ablation studies, we provide empirical evidence on the impact of different sensing modality combinations on prediction performance. This analysis reveals that modality diversity generally enhances prediction accuracy, offering new insights into the value of multimodal fusion in beam prediction and advancing the understanding of multi-source data contributions in this domain.

The rest of this paper is organized as follows: Section II establishes the system model and problem formulation of V2I mmWave beam prediction. The proposed M²BeamLLM framework is presented in Section III. Section IV presents extensive simulation results, including performance comparisons with other methods, along with some ablation studies. Finally, we conclude our work in Section V.

Notations: Bold lowercase letters denote vectors (e.g., \mathbf{x}), and bold uppercase letters denote matrices (e.g., \mathbf{X}). The superscripts $(\cdot)^T$ and $(\cdot)^H$ represent the transpose and Hermitian (conjugate transpose) operations, respectively. The symbol \oslash denotes element-wise division. The operator $\mathbb{E}[\cdot]$ denotes the statistical expectation, while $|\cdot|_2$ denotes the Euclidean norm of a vector, and $|\cdot|$ returns the magnitude of a complex number. The functions $\min(\cdot)$ and $\max(\cdot)$ return the minimum and maximum element, respectively. The indicator function $\mathbb{1}\{\cdot\}$ equals 1 if the condition inside the braces is true, and 0 otherwise. Unless otherwise specified, \mathbb{R} and \mathbb{C} denote the sets of real and complex numbers, respectively.

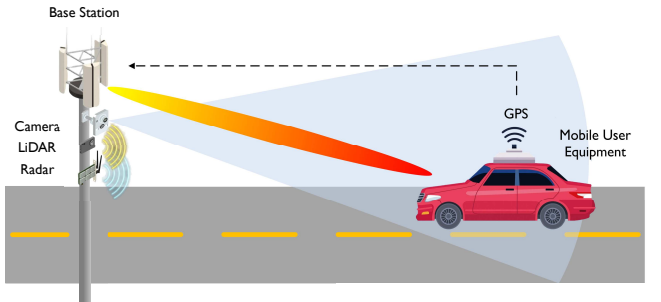


Fig. 1: Illustration of the V2I system model: The BS is equipped with a camera, radar, and LiDAR, while a GPS-RTK system provides the UE's localization information to the BS.

II. SYSTEM MODEL AND PROBLEM FORMULATION

A. System Model

As shown in Fig. 1, without loss of generality, we consider a wireless communication system with N -antenna BS and a single-antenna UE, employing a pre-defined beamforming codebook denoted as $\mathcal{F} = \{\mathbf{f}_m\}_{m=1}^M$, where $\mathbf{f}_m \in \mathbb{C}^{N \times 1}$ represents the m -th beamforming vector in the codebook. At time instance t , the transmitter selects a beam $\mathbf{f}_{m[t]} \in \mathcal{F}$ for signal transmission, where $m[t]$ denotes the index of the

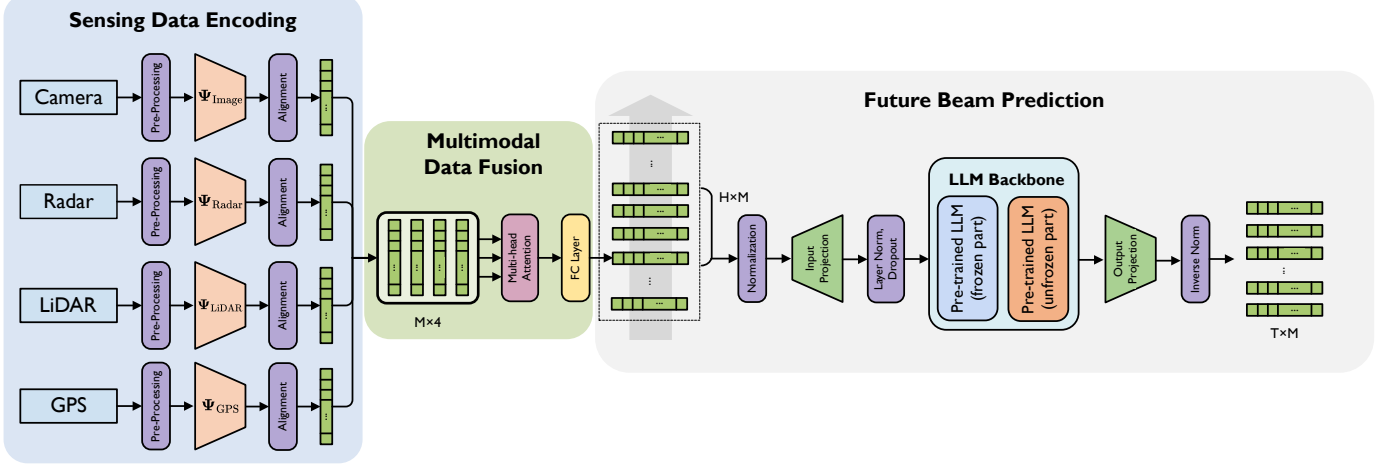


Fig. 2: The model framework of M²BeamLLM. In the sensing data encoding part, it encodes and aligns multimodal sensing data from camera, radar, LiDAR, and GPS. It then fuses these diverse inputs using a multi-head attention mechanism. Subsequently, the fused data undergoes input projection before being fed into an LLM backbone, which includes both frozen and unfrozen pre-trained components. Finally, an output projection and inverse normalization are applied to predict future beams.

beamforming vector at time instant t . The received signal is modeled as

$$\mathbf{y}[t] = \mathbf{h}^H[t] \mathbf{f}_{m[t]} s + n[t]. \quad (1)$$

where $\mathbf{h}[t]$ is the mmWave channel vector, s is the unit-power transmitted symbol, and $n[t] \sim \mathcal{CN}(0, \sigma_n^2)$ is complex additive Gaussian noise. The optimal beam selection strategy maximizes the effective channel gain as follows:

$$\mathbf{f}_{m^*[t]} = \arg \max_{m \in \{1, \dots, M\}} |\mathbf{h}^H[t] \mathbf{f}_{m[t]}|^2, \quad (2)$$

where $m^*[t]$ denotes the index of the optimal beamforming vector at time instant t . This selection criterion ensures the highest possible received signal-to-noise ratio (SNR) under the given codebook constraints.

B. Problem Formulation

We aim to design a beam prediction strategy that maximizes the probability of correctly identifying the optimal beam index $m^*[t]$ over a future horizon $t = 1, 2, \dots, T$, leveraging historical observations from time slots $\tau = -H+1, -H+2, \dots, 0$. The performance metric is defined as the expected accuracy over T :

$$\mathcal{P} = \mathbb{E} \left[\frac{1}{T} \sum_{t=1}^T \mathbb{1}\{\hat{m}[t] = m^*[t]\} \right], \quad (3)$$

where the expectation is taken over the joint distribution of channel realizations $\{\mathbf{h}[t]\}_{t=1}^T$ and historical observations $\{\mathbf{h}[\tau]\}_{\tau=-H+1}^0$. While this formulation relies on temporal correlations in channel realizations, such methods face the following fundamental limitations:

- **Channel dynamics dependency:** Traditional approaches assume predictable temporal patterns (e.g., slow fading, Markovian transitions), which collapse in non-stationary scenarios (e.g., sudden blockage by vehicles, UAV swarms maneuvering).

- **Reactive adaptation:** Channel measurements only provide posterior information, delaying beam adjustments until after link degradation occurs.

In contrast, sensing data enables proactive prediction by directly observing the physical causes of channel variations. This paradigm shift replaces statistical channel extrapolation with geometric-environmental reasoning, achieving robustness against abrupt channel dynamics through environment-aware prediction.

III. M²BEAMLLM FRAMEWORK

In this section, we introduce M²BeamLLM to tackle the multimodal sensing data empowered beam prediction task outlined in Section II. The general M²BeamLLM framework is shown in Fig. 2, which consists of the following key components: sensing data encoding, multimodal data fusion, and future beam prediction.

A. Multimodal Feature Encoding

The BS is equipped with a set of sensing modalities denoted by $\Omega = \{\text{Image}, \text{Radar}, \text{LiDAR}, \text{GPS}\}$. For each modality $\omega \in \Omega$, the raw sensing data at time t is represented as $\mathbf{X}_\omega[t]$, with the following specifications:

- **Image Data:** $\mathbf{X}_{\text{Image}}[t] \in \mathbb{R}^{W_I \times H_I \times C_I}$, where W_I , H_I and C_I represent the spatial width, height, and RGB/IR spectral channels, respectively.
- **Radar Data:** $\mathbf{X}_{\text{Radar}}[t] \in \mathbb{C}^{M_R \times S_R \times A_R}$, where the dimensions correspond to antenna, sampling, and chirp, providing information on the target's angle, distance, and velocity.
- **LiDAR Data:** $\mathbf{X}_{\text{LiDAR}}[t] \in \mathbb{R}^{N_L[t] \times 3}$, with $N_L[t]$ being the time-varying number of 3D points (x, y, z) in the LiDAR point cloud.
- **GPS Data:** $\mathbf{X}_{\text{GPS}}[t] \in \mathbb{R}^{2 \times 1}$, containing the latitude and longitude coordinates of the UE. Although GPS data incurs uplink latency from UE to the BS, its computational

simplicity compared to other latency-intensive modalities enables synchronization via buffer delay or some other schemes.

We formalize the feature extraction process for each sensing modality, where $\Psi_\omega(\cdot)$ denotes the modality-specific feature encoder for $\omega \in \Omega$. Their specific architecture is shown in Fig. 3. A detailed description is given below:

1) *Image Data Feature Extraction*: The image feature extraction pipeline processes raw input $\mathbf{X}_{\text{Image}}[t]$ through three stages: standardization, backbone processing, and dimension compression. First, each image is reshaped to $224 \times 224 \times 3$ and normalized using ImageNet parameters [16]:

$$\mathbf{x}_{\text{Image}}^{\text{Norm}} = (\text{Reshape}(\mathbf{X}_{\text{Image}}[t]) - \boldsymbol{\mu}_{\text{Image}}) \odot \boldsymbol{\sigma}_{\text{Image}}, \quad (4)$$

where $\text{Reshape}(\cdot)$ represents image reshaping operation, $\boldsymbol{\mu}_{\text{Image}}$ and $\boldsymbol{\sigma}_{\text{Image}}$ are the mean and standard deviation of the ImageNet dataset, respectively.

The normalized tensor is then fed into a pretrained ResNet-18 backbone [17] (with removed classification layers), followed by a learnable fully connected (FC) layer that compresses features to M dimensions:

$$\tilde{\mathbf{x}}_{\text{Image}}[t] = \Psi_{\text{Image}}(\mathbf{x}_{\text{Image}}^{\text{Norm}}) \in \mathbb{R}^M. \quad (5)$$

2) *Radar Data Feature Extraction*: The radar feature extraction pipeline begins by processing raw radar data $\mathbf{X}_{\text{Radar}}[t]$ through a two-dimensional fast Fourier transform (2D-FFT) applied to each chirp signal along the antenna and fast-time dimensions. This transformation generates a range-angle (RA) map:

$$\mathbf{X}_{\text{Radar}}^{\text{RA}}[t] = \sum_{a=1}^{A_R} |\text{FFT}_{2\text{D}}(\mathbf{X}_{\text{Radar}}[t][:, :, a])| \in \mathbb{R}^{M_F \times S_R}, \quad (6)$$

where $\text{FFT}_{2\text{D}}(\cdot)$ represents the 2D-FFT operation. The antenna dimension is zero-padded from M_R to M_F ($M_F > M_R$) to achieve angular oversampling, reducing the effective angular sampling interval and enhancing spectral detail resolution [18]. The resulting RA map is then encoded into a feature vector through a convolutional neural network [19]:

$$\tilde{\mathbf{x}}_{\text{Radar}}[t] = \Psi_{\text{Radar}}(\mathbf{X}_{\text{Radar}}^{\text{RA}}[t]) \in \mathbb{R}^M. \quad (7)$$

3) *LiDAR Data Feature Extraction*: The LiDAR feature extraction pipeline processes raw point cloud data $\mathbf{X}_{\text{LiDAR}}[t]$ through geometric transformation and neural encoding. First, the 3D points are projected onto a 256×256 2D grid to create a histogram representation $\mathbf{X}_{\text{LiDAR}}^{\text{Hist}}[t]$, where point counts per cell are clipped to 5 and normalized to $[0, 1]$ for robustness:

$$\mathbf{X}_{\text{LiDAR}}^{\text{Hist}}[t] = \text{PC2H}(\mathbf{X}_{\text{LiDAR}}[t]) \in \mathbb{R}^{1 \times 256 \times 256}, \quad (8)$$

where $\text{PC2H}(\cdot)$ denotes the point-cloud-to-histogram transformation. This single-channel feature map is then encoded into an M -dimensional feature vector using a modified ResNet-18 architecture:

$$\tilde{\mathbf{x}}_{\text{LiDAR}}[t] = \Psi_{\text{LiDAR}}(\mathbf{X}_{\text{LiDAR}}^{\text{Hist}}[t]) \in \mathbb{R}^M, \quad (9)$$

4) *GPS Data Feature Extraction*: The GPS feature extraction process begins by normalizing raw coordinate data \mathbf{X}_{GPS} to ensure compatibility with subsequent fusion operations. Using min-max scaling applied across the entire historical dataset $\mathbf{X}_{\text{GPS}} \in \mathbb{R}^{2 \times H}$, we maintain temporal consistency through global normalization:

$$\mathbf{X}_{\text{GPS}}^{\text{Norm}}[t] = \frac{\mathbf{X}_{\text{GPS}}[t] - \min(\mathbf{X}_{\text{GPS}})}{\max(\mathbf{X}_{\text{GPS}}) - \min(\mathbf{X}_{\text{GPS}})}. \quad (10)$$

The normalized coordinates are then mapped to an M -dimensional feature space through a multilayer perceptron (MLP) network:

$$\tilde{\mathbf{x}}_{\text{GPS}}[t] = \Psi_{\text{GPS}}(\mathbf{X}_{\text{GPS}}^{\text{Norm}}[t]) \in \mathbb{R}^M. \quad (11)$$

B. Multimodal Alignment

Multimodal alignment seeks to bridge the semantic discrepancies among heterogeneous sensing modalities by projecting modality-specific features into a shared embedding space, thereby enabling effective cross-modal fusion [20]. In this work, we employ a contrastive learning-based alignment strategy inspired by CLIP [21], which enforces geometric consistency among modalities through cosine similarity constraints. Specifically, the feature vector $\tilde{\mathbf{x}}_\omega[t]$ extracted from each modality $\omega \in \Omega$ at time step t is first ℓ_2 -normalized:

$$\bar{\mathbf{x}}_\omega[t] = \frac{\tilde{\mathbf{x}}_\omega[t]}{\|\tilde{\mathbf{x}}_\omega[t]\|_2}, \quad \forall \omega \in \Omega, \quad (12)$$

projecting all features onto the unit hypersphere \mathbb{S}^{M-1} . This normalization facilitates stable optimization using cosine similarity as the alignment metric. Cross-modal alignment is then enforced by maximizing the pairwise cosine similarity between normalized feature vectors. These similarities are organized into a symmetric matrix $\mathbf{S}[t] \in [-1, 1]^{|\Omega| \times |\Omega|}$, where each element is computed as

$$S_{\omega_1, \omega_2}[t] = \bar{\mathbf{x}}_{\omega_1}[t] \bar{\mathbf{x}}_{\omega_2}^\top[t], \quad \forall \omega_1, \omega_2 \in \Omega \quad (13)$$

which quantitatively reflects the semantic consistency between modalities ω_1 and ω_2 at time t .

By encouraging high cross-modal similarity, this geometric constraint implicitly disentangles modality-invariant semantics from modality-specific noise, thereby enabling robust and generalizable feature fusion—especially under distributional shifts or missing modalities.

C. Multimodal Feature Fusion

To integrate features from heterogeneous modalities, we design a transformer-based fusion module that captures cross-modal dependencies through self-attention mechanisms. For each time step t , the normalized features $\{\tilde{\mathbf{x}}_\omega[t]\}_{\omega \in \Omega}$ are stacked into a matrix $\mathbf{F}[t] = [\tilde{\mathbf{x}}_{\text{Image}}^\top[t], \tilde{\mathbf{x}}_{\text{Radar}}^\top[t], \tilde{\mathbf{x}}_{\text{LiDAR}}^\top[t], \tilde{\mathbf{x}}_{\text{GPS}}^\top[t]]^\top \in \mathbb{R}^{M \times 4}$, where each row corresponds to a modality. To model inter-modal interactions, we apply a multi-head self-attention operation, where the queries, keys, and values are all set to $\mathbf{F}^\top[t]$, i.e., $Q(t) = K(t) = V(t) = \mathbf{F}^\top[t]$:

$$\mathbf{A}[t] = \text{MultiHead}(\mathbf{F}^\top[t], \mathbf{F}^\top[t], \mathbf{F}^\top[t]) \in \mathbb{R}^{|\Omega| \times M}. \quad (14)$$

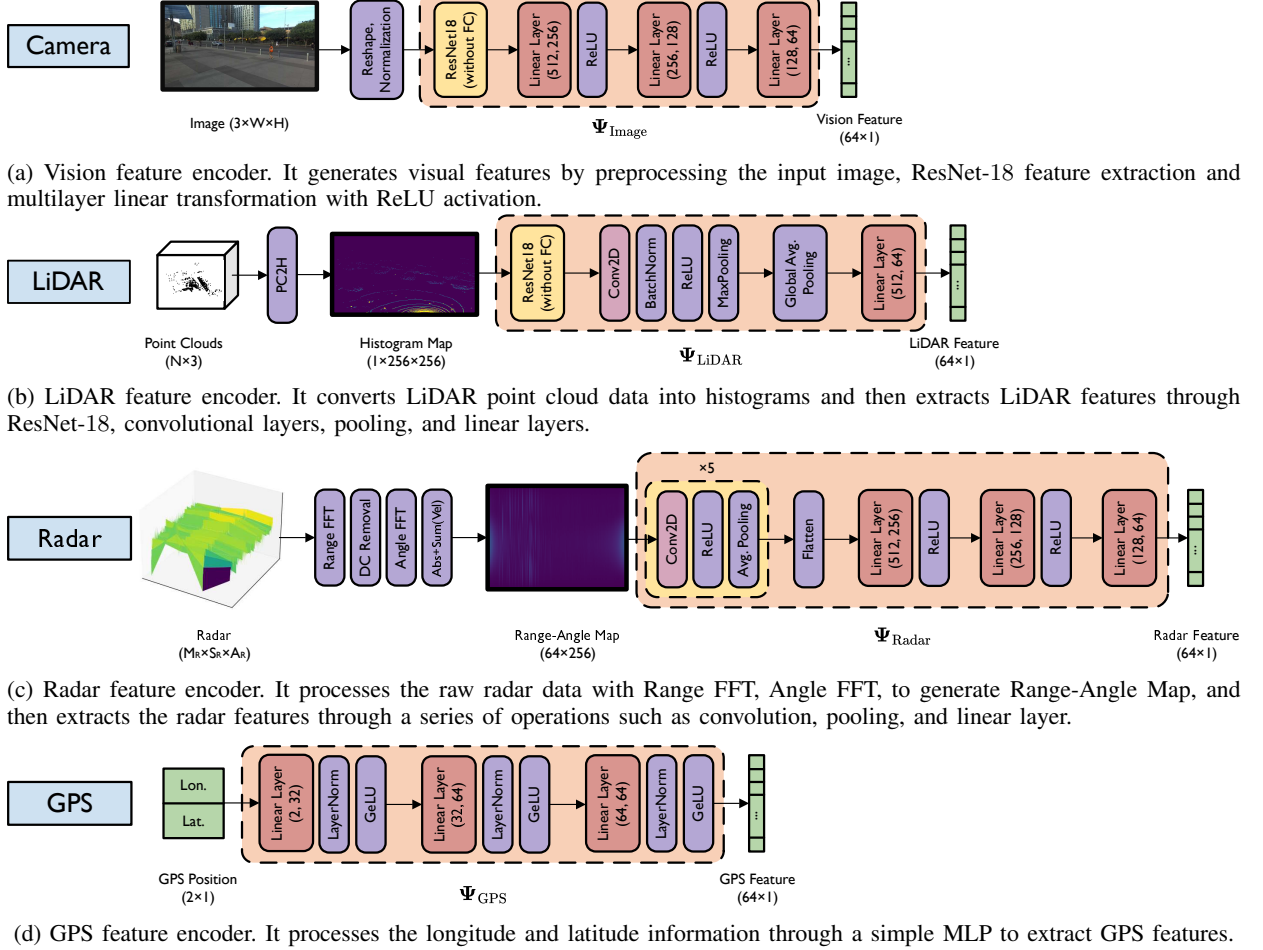


Fig. 3: Multimodal data encoding module for the M²BeamLLM system. This module demonstrates in detail the independent feature encoding process for (a) camera, (b) LiDAR, (c) radar, and (d) GPS sensors, converting the raw sensor data into a unified feature representation for subsequent multimodal data fusion.

Each attention head captures distinct correlation patterns among modalities, and the outputs are concatenated and projected back to the original dimension M . This enables dynamic weighting and context-aware fusion of modality-specific features. The modality-aware representations are then aggregated across modalities by summing the attended vectors:

$$\mathbf{z}[t] = \text{FFN} \left(\sum_{\omega \in \Omega} \mathbf{A}[t]_{(\omega, :)} \right) \in \mathbb{R}^M, \quad (15)$$

where $\text{FFN}(\cdot)$ denotes a position-wise feed-forward network (FFN) that refines the fused representation. Finally, the time-series feature sequence is formed by concatenating the fused embeddings over a historical window of length H :

$$\mathbf{Z} = [\mathbf{z}[-H+1], \mathbf{z}[-H+2], \dots, \mathbf{z}[0]]^T \in \mathbb{R}^{H \times M}, \quad (16)$$

which serves as the input to downstream temporal modeling modules for beam prediction.

D. Prediction

The fused sequence obtained from the previous steps is fed into a prediction network $\text{Pred}(\cdot)$ to make predictions, as

follows:

$$\hat{\mathbf{P}} = \text{Pred}(\mathbf{Z}) \in \mathbb{R}^{T \times M}. \quad (17)$$

Finally, for each time sample t , we can choose the optimal beam index for prediction:

$$\hat{m}[t] = \arg \max_m \hat{\mathbf{P}}[t, m]. \quad (18)$$

E. Model Structure

Input Projection. Given an input feature sequence \mathbf{Z} , the input embedding module is designed to project \mathbf{Z} into a d_{LLM} -dimensional embedding space, effectively treating each time step as a token embedding suitable for LLMs. In other words, this process enables LLMs to “comprehend” the input feature sequence. Prior to embedding, \mathbf{Z} is normalized to have zero mean and unit variance, which stabilizes training and preserves the relative relationships between features. The normalized sequence is then linearly transformed into variable-length embeddings compatible with the LLM input format.

Pretrained LLM and SFT. We employ a pretrained LLM backbone, freezing most of its self-attention and feed-forward layers during fine-tuning to retain the general representations

learned from large-scale data. To enable task adaptation, the parameters of the last few layers are unfrozen and updated. This selective fine-tuning strategy balances model stability and plasticity: it mitigates overfitting risks on relatively small datasets while allowing higher layers to specialize in task-specific refinements without degrading the foundational knowledge captured in lower layers. In M²BeamLLM, this strategy is applied to beam prediction via SFT, requiring only a small amount of labeled data from the target task. By freezing the majority of layers, our approach efficiently adapts the pretrained LLM to the specific demands of beam prediction in mmWave systems, while significantly reducing the training cost.

Output Projection. The contextualized embeddings output by the LLM are projected back to the original feature dimension M through a learnable linear layer, producing the final predictions aligned with the input feature space.

F. Learning Phase

The training process consists of two parts: encoder pre-training and beam prediction module fine-tuning. The encoder pre-training simply takes the one-hot encoding vector corresponding to the modal input with the optimal beam index as a supervised learning pair and then performs M classification with the following loss function:

$$\mathcal{L}_{\text{enc}} = - \sum_{m=1}^M p_m \log(\sigma_{\text{Softmax}}(\hat{p}_m)), \quad (19)$$

where $p_m \in \{0, 1\}$ denotes the ground-truth one-hot encoded optimal beam index, \hat{p}_m represents the model prediction probability for the m -th beam, and $\sigma_{\text{Softmax}}(\cdot)$ is the softmax activation function.

For beam prediction module fine-tuning part, the composite loss function comprises two key objectives:

1) *Prediction Task Objective*: We optimize beam index prediction accuracy through cross-entropy loss defined as:

$$\mathcal{L}_1 = - \frac{1}{T} \sum_{t=1}^T \sum_{m=1}^M p_m[t] \log(\sigma_{\text{Softmax}}(\hat{p}_m[t])). \quad (20)$$

2) *Multimodal Alignment Objective*: Inter-modal feature similarity is enforced via normalized temperature-scaled contrastive loss defined as:

$$\mathcal{L}_2 = - \frac{\sum_{\tau=-H+1}^0 \sum_{\omega_1, \omega_2 \in \Omega} p_m[t] \log \left(\sigma_{\text{Softmax}} \left(\frac{S_{\omega_1, \omega_2}[t]}{\alpha} \right) \right)}{H \cdot |\Omega|(|\Omega| - 1)} \quad (21)$$

where temperature parameter $\alpha > 0$ modulates similarity concentration: smaller α sharpens hard negative mining while larger α promotes softer distribution.

3) *Composite Optimization Objective*: The unified training loss is defined by combining both objectives with weight $\lambda \in [0, +\infty)$ as follows:

$$\mathcal{L} = \mathcal{L}_1 + \lambda \mathcal{L}_2. \quad (22)$$

TABLE I: Default Parameter Settings.

Parameters	Value
Scenario	DeegSense 6G Scenario 32
W_I, H_I, C_I	960, 540, 3
M_R, S_R, A_R	4, 256, 128
N_L	~ 18000
μ_{Image}	[0.485, 0.456, 0.406]
σ_{Image}	[0.229, 0.224, 0.225]
d_{LLM}	768
α	0.07
λ	1
Number of unfrozen layers	2

IV. SIMULATION RESULTS

A. Experimental Settings

1) *Dataset Processing*: In this study, we employ the DeepSense 6G dataset [22] to simulate a V2I mmWave communication environment. In this configuration, a stationary BS is equipped with an array of sensing technologies, including an RGB camera, radar, and LiDAR sensor, which collectively interact with a mobile UE functioning as a mmWave transmitter. The UE incorporates a GPS-RTK system that continuously streams meter-accurate positional data to the BS.

The dataset is partitioned into training (70%, 2,138 samples) and testing (30%, 917 samples) sets, where each sample represents a complete vehicle pass-by event comprising synchronized multimodal sensing data sequences and beam index sequences. We decompose each sequence into input-output pairs using a 13-frame sliding window, configuring two prediction tasks: 1) standard prediction with $H = 8$ historical observations and $T = 5$ future beams, and 2) few-shot prediction with $H = 3$ and $T = 10$, where the model processes multimodal sensing data inputs $\{\tilde{\mathbf{x}}_{\text{Image}}[t], \tilde{\mathbf{x}}_{\text{LiDAR}}[t], \tilde{\mathbf{x}}_{\text{Radar}}[t], \tilde{\mathbf{x}}_{\text{GPS}}[t]\}_{\tau=-H+1}^0$ while learning illumination-robust environment-beam correlations.

2) *Baselines*: The default LLM backbone used in M²BeamLLM is the distilled GPT-2 model [23]. As a long-standing benchmark and representative of encoder-based architectures, BERT is selected as the primary comparison baseline.¹ We compare our approach with several time-series forecasting models, including RNN-based model (GRU [24], LSTM [25]), linear model (NLinear [26]), and transformer-based model (Informer [27]).

3) *Implementation Settings*: Our experiments are conducted on a single NVIDIA A100-40 GB GPU via Google Colab, implemented in PyTorch. We employ the Adam optimizer [28] with an initial learning rate of 10^{-3} , which decays by a factor of 0.5 every 5 epochs, alongside a batch size of 16 and a training duration over 30 epochs. The remaining simulation parameters are listed in Table I.

4) Performance Metrics

- **Top- K Accuracy**: It measures whether the true label is included among the top- K predicted beamforming

¹Both models are publicly available on the Hugging Face, with the respective URLs as follows: <https://huggingface.co/tanyildizderya/distilled-gpt2> and <https://huggingface.co/google-bert/bert-base-uncased>.

vectors with the highest probabilities, defined as:

$$\text{Top-}K \text{ Accuracy} = \frac{1}{N_{\text{Test}}} \sum_{n=1}^{N_{\text{Test}}} \mathbb{1}\{m_n \in \mathcal{Q}_K\}, \quad (23)$$

where N_{Test} represents the total number of samples in the test set, m_n denotes the index of the ground truth optimal beam for the n -th sample, and \mathcal{Q}_K is the set of indices for the top K predicted beams, sorted by the element values in $\hat{\mathbf{P}}$ for each time sample.

- **Distance-Based Accuracy (DBA) Score:** It measures the accuracy of the distance between the predicted beam and the ground truth beam. For this, we utilize the top- K predicted beams. The DBA-Score is defined as

$$\text{DBA-Score} = \frac{1}{K} \sum_{k=1}^K Y_k, \quad (24)$$

where

$$Y_k = 1 - \frac{1}{N_{\text{Test}}} \sum_{n=1}^{N_{\text{Test}}} \min_{1 \leq k' \leq k} \left[\min \left(\frac{|m_n - \hat{m}_{n,k'}|}{\Delta}, 1 \right) \right]. \quad (25)$$

Here, $\hat{m}_{n,k'}$ represents the prediction for the k -th most-likely beam index of sample n , and Δ is a normalization factor. Unlike traditional top- K accuracy that focus on whether a prediction hits the target, it introduces a “precision-aware” evaluation criterion that allows for distance errors. If the prediction is close but not entirely correct, it can still receive a favorable score.

To facilitate presentation, the two performance metrics in the simulation results are averaged over all predicted time sequences.

B. Dataset Analysis and Visualization

In this section, we present an analysis and visualization of the dataset used. For visual and GPS data, we visualize multiple samples due to the significant variation between different instances. In contrast, Radar and LiDAR data exhibit less variation across samples; therefore, we provide a single sample visualization as a representative example.

Fig. 4 shows the frequency with which each beam index was optimal in the dataset in Scenario 32. We observed that optimal beam indices in the range of 10 to 30 occur with higher frequency, with a particularly prominent peak around index $m^* = 17$.

Fig. 5 illustrates the relative received power distribution across various beam indices (20, 40, 60) for the first three samples, highlighting how peak power varies with different beam selections. Note that due to the complexity of absolute power calibration, the DeepSense 6G dataset provides dimensionless relative received signal power [22]. From the figure, it can be seen that as the optimal beam index increases, the relative received power shows an overall increasing trend. With a beam index of 20, the peak of the relative received power is around 0.25; with a beam index of 40, the peak of the relative received power improves to around 0.4; and when the beam index is 60, the relative received power reaches the highest

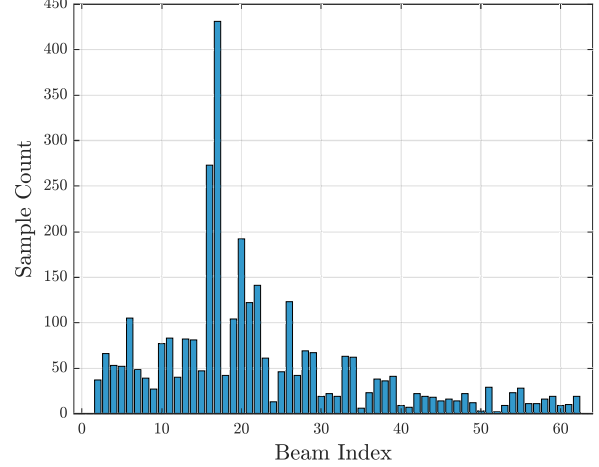


Fig. 4: Optimal beam index frequency distribution.

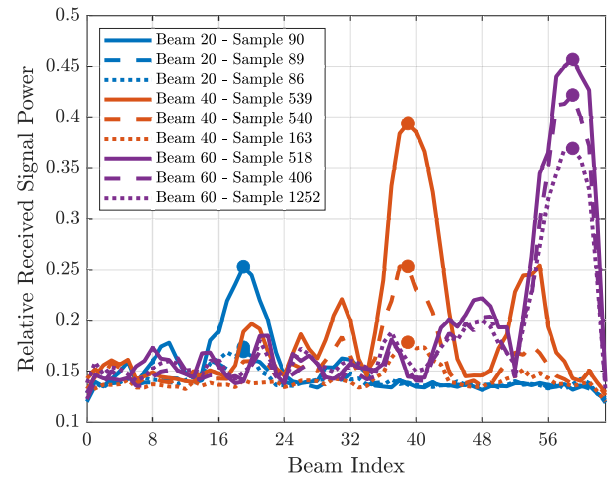


Fig. 5: Comparison of power profiles for the first 3 samples associated with optimal beams 20, 40, and 60, respectively.

level of around 0.45. This implies that the distance between transceivers in the dataset may be smaller when the beam index is larger, leading to an increase in received power.

Fig. 6 shows the first three samples when the optimal beam is 20, 40, and 60, respectively. Notice that the UE is the gray car with the sensor at the top, and the optimal beam index gets progressively larger as it travels from the left side of the screen over to the right side. For example, in samples 540 and 163, the UE locations are nearly identical, but the weather conditions differ. As shown in Fig. 5, this leads to noticeable differences in the received power. From this we can see that the weather condition affects the received power.

Fig. 7 shows two subplots of sample 86: (a) the RA map and (b) the range-velocity (RV) map, both of which indicate signal energy in terms of color intensity. The radar system successfully detected multiple objects within the environment. A significant portion of these detected objects appear to be either stationary, functioning as environmental scatterers, or moving very slowly, such as pedestrians. This is clearly substantiated



(a) Vision data visualization for the first 3 samples associated with optimal beam 20.

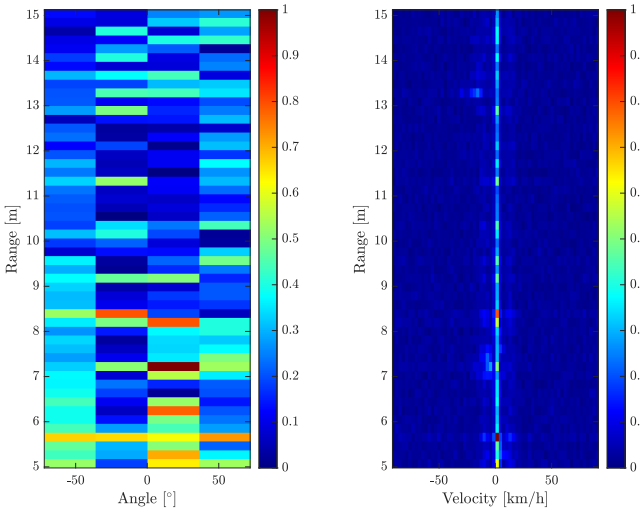


(b) Vision data visualization for the first 3 samples associated with optimal beam 40.



(c) Vision data visualization for the first 3 samples associated with optimal beam 60.

Fig. 6: Vision data visualization for the first 3 samples associated with optimal beams 20, 40, and 60, respectively.



(a) Range-angle map of sample 86. (b) Range-velocity map of sample 86.

Fig. 7: Radar data visualization of sample 86.

by their distinct positions in the angle-distance spectrum and their strong concentration along the 0 velocity line in the RV map. Furthermore, the radar system is also capable of identifying distinct moving targets at specific distances. For instance, at a range of approximately 7 meters, the clear angular and velocity information collectively indicates the presence of a moving target that the radar system is actively tracking.

Fig. 8 represents the point cloud data of objects or environments in 3D space for sample 86, which, although sparse, reveals the presence of one or more major structures, such as trees, buildings, driveways, etc.

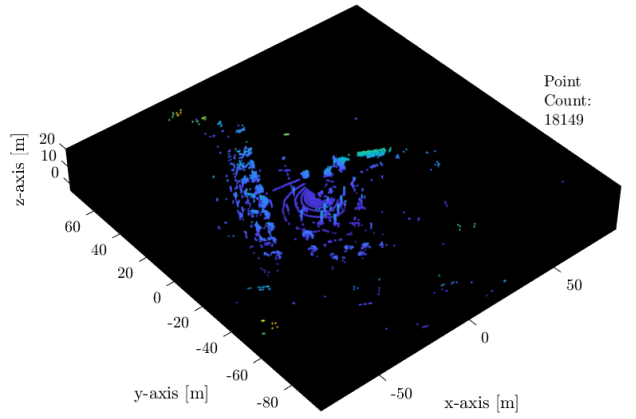


Fig. 8: Visualization of LiDAR point cloud data of sample 86.

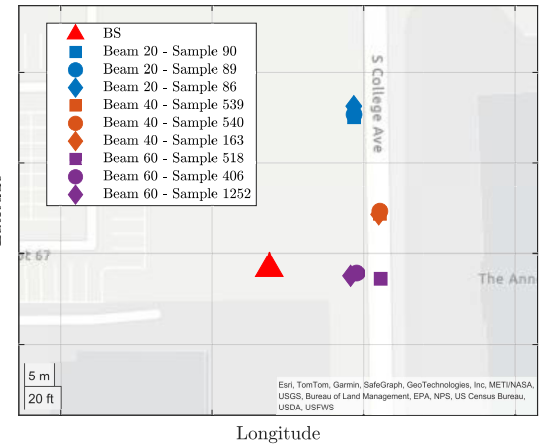


Fig. 9: BS and UE GPS location map for the first 3 samples associated with optimal beams 20, 40, and 60, respectively.

Fig. 9 is a geolocation map to show the GPS location of the top three samples with optimal beam indexes of 20, 40, and 60. Combined with the analysis from Fig. 6, we find that the positional and visual information basically remain aligned.

C. Standard Prediction

Fig. 10 presents a comparative analysis of Top-1, Top-2, and Top-3 accuracy for standard beam predictions across all evaluated models. As expected, increasing the value of K leads to improved accuracy for all models, as the correct label is more likely to appear within the top- K candidates. Despite the large number of parameters, we only activated a small fraction for SFT, so we attribute the high performance to the successful knowledge activation of LLM. Notably, the proposed GPT-2-based M²BeamLLM achieves the highest Top-1 accuracy of 68.9%, surpassing the second-best model, BERT-based M²BeamLLM (55.0%), by a substantial 13.9%. This significant margin highlights the superior suitability of the transformer decoder architecture (e.g., autoregressive masking

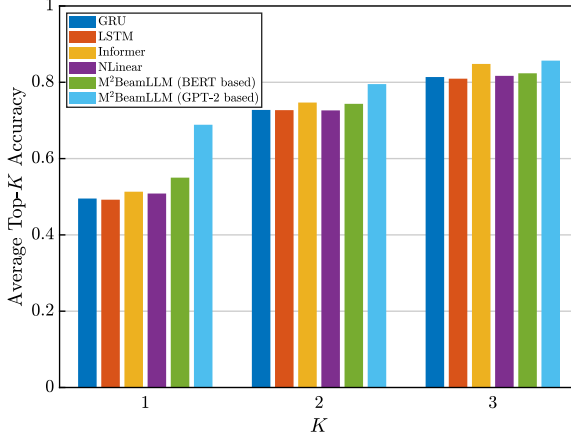


Fig. 10: Average Top- K accuracy performance of the proposed method comparing to several baselines in the standard prediction task.

in GPT-2) for future beam index prediction, compared to the bidirectional encoder architecture used in BERT. Traditional RNN-based models show relatively weak performance at $K = 1$, but exhibit notable gains at higher K values. This suggests that while RNNs may struggle to rank the most likely beams correctly, they still offer reasonable overall coverage among top predictions. The Informer model approaches GPT-2-based performance at $K = 3$, illustrating the strength of its attention mechanism in capturing long-range dependencies. Meanwhile, the simple NLinear model performs comparably to RNNs, reflecting the surprising effectiveness of linear models when trained with sufficient data.

Fig. 11 presents the DBA-score as a complementary metric to further differentiate model performance and their temporal alignment behavior under varying tolerance thresholds. As observed, all models demonstrate a progressive improvement in performance as the top- K value increases (from 1 to 5) and the tolerance threshold Δ is relaxed (from 1 to 2), indicating greater flexibility in acceptable prediction errors. However, the extent of this improvement is highly architecture-dependent. The proposed GPT-2-based M²BeamLLM consistently achieves the highest DBA-scores across all settings, further confirming its robust capability in both beam prediction accuracy. As the tolerance is relaxed to $\Delta = 2$, the performance gap between models becomes noticeably smaller. This suggests that a more permissive evaluation criterion reduces the sensitivity to exact temporal alignment, thereby diminishing the relative advantage of more sophisticated models under looser error constraints.

D. Few-Shot Prediction

In Figs. 12 and 13, we present the top- K accuracy and DBA-score performance for the few-shot prediction task. It is important to note that at this point $H < T$, we need to pad the input of M²BeamLLM with zeros to extend it to T in the time dimension. Despite the overall performance decline, M²BeamLLM continues to exhibit superior performance, maintaining its leading position among the evaluated

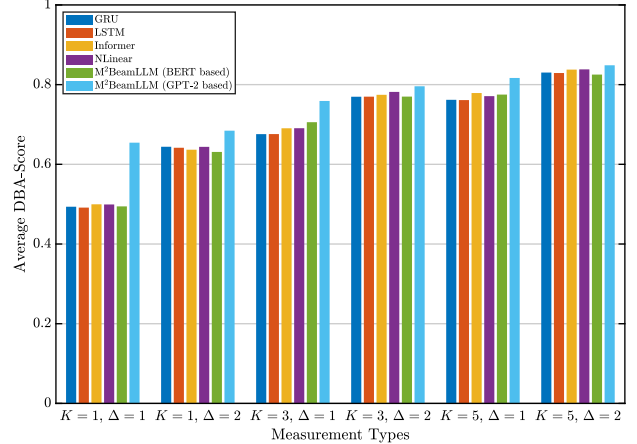


Fig. 11: Average DBA-score performance of the proposed method comparing to several baselines in the standard prediction task.

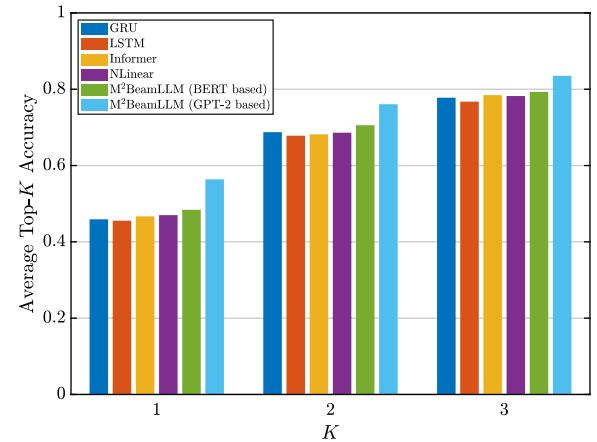


Fig. 12: Average Top- K accuracy performance of the proposed method comparing to several baselines in the few-shot prediction task.

models. However, the Top-2 and Top-3 accuracy metrics remain largely unaffected.

E. Comparative Analysis and Component Ablation Study

In this section, we conduct a series of ablation studies to validate the effectiveness and superiority of the proposed M²BeamLLM framework. Specifically, we design experiments to investigate two key aspects: (1) the impact of different modality combinations on beam prediction performance, and (2) the influence of the number of frozen layers in the pre-trained LLM during supervised fine-tuning.

1) *Comparative Analysis of Different Modalities*: We focus on evaluating the performance impact of different combinations of sensing modalities. This analysis investigates how varying the number of input modalities influences beam prediction accuracy. The training and evaluation results are presented in Figs. 14, 15, and 16, showcasing performance across three single-modality, two dual-modality, one tri-modality, and

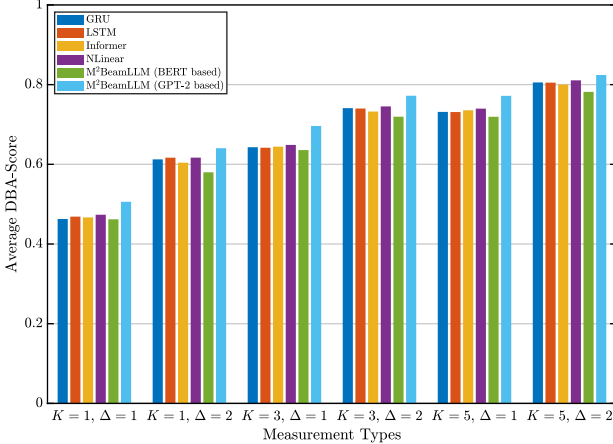


Fig. 13: Average DBA-score performance of the proposed method comparing to several baselines in the few-shot prediction task.

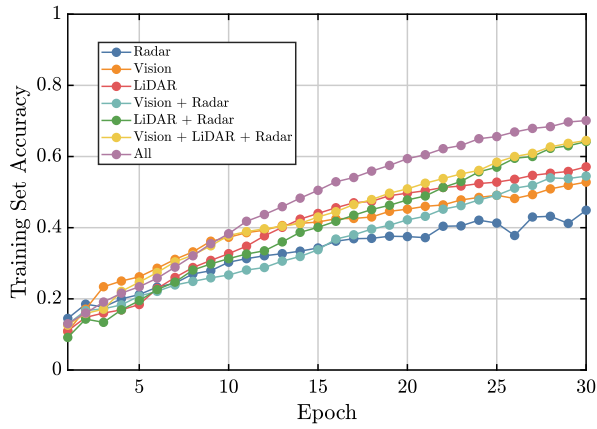


Fig. 14: Top-1 training accuracy performance comparison of different combinations of sensing data.

one full-modality configurations. A clear trend of performance enhancement through multimodal fusion emerges, where an increased number of modalities generally leads to improved beam prediction accuracy. For instance, in terms of Top-1 accuracy, the combination of vision and radar modalities achieves an accuracy of 51.1%, representing an improvement of 2.6% and 13.1% over using vision-only and radar-only modalities, respectively. Further incorporating the LiDAR modality boosts the accuracy by an additional 10.7%. Building upon this improvement, the inclusion of GPS data yields a further 7.1% gain in accuracy. These results highlight the complementary benefits of multimodal sensing and validate the effectiveness of the proposed M²BeamLLM framework in leveraging diverse sensing inputs for robust and accurate beam prediction.

2) Comparative Analysis of the Performance of Different Frozen Pre-training Layers: In this section, we explore the impact of unfreezing different numbers of layers in the LLM backbone model on training and performance.

We observe that as more transformer layers are unfrozen,

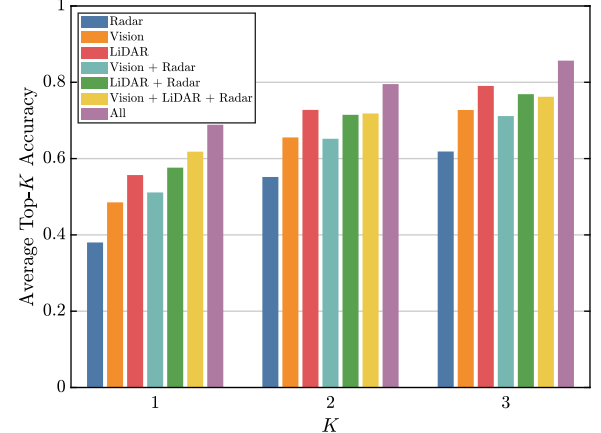


Fig. 15: Average Top- K accuracy performance of different combinations of sensing data.

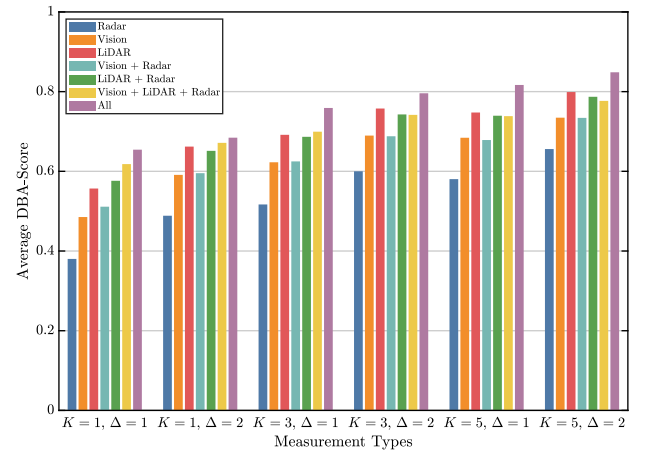


Fig. 16: Average DBA-score performance of different combinations of sensing data.

the number of trainable parameters increases from 62.3 M (0 layers) to 147.3 M (12 layers), with the final validation loss decreasing from 1.52 to 0.21 after 30 epochs. Top- K accuracies and DBA-scores consistently improve with deeper fine-tuning. For instance, Top-1 accuracy increases from 47.4% (0 layers) to 85.7% (12 layers), while DBA-score with Top-1, $\Delta = 1$ reaches 0.94 at full fine-tuning. These results demonstrate that deeper fine-tuning not only improves convergence but also enhances semantic and temporal alignment of predictions.

Furthermore, even partial fine-tuning provides substantial gains: unfreezing just 4 layers results in significant improvements across all metrics (e.g., Top-1 accuracy from 47.4% \rightarrow 72.4%, DBA-score with Top-1, $\Delta = 1$ from 0.47 \rightarrow 0.72). Deeper tuning beyond 8 layers continues to yield improvements, though with diminishing returns relative to computational cost.

If computational resources allow, we recommend full fine-tuning (12 layers) to achieve optimal performance. For resource-constrained scenarios (e.g., limited GPU memory or training time), unfreezing 6–8 layers strikes a highly cost-

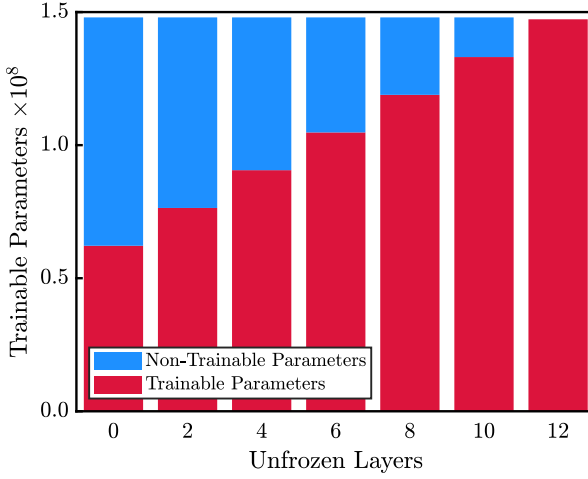


Fig. 17: Distribution of trainable versus non-trainable parameters across unfrozen layers.

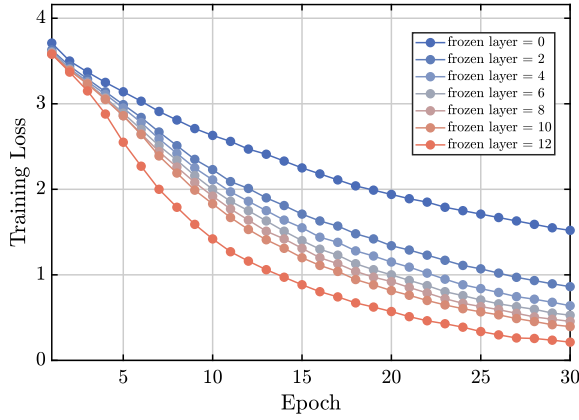


Fig. 18: Effect of the number of frozen layers on training loss.

effective balance, achieving Top-3 accuracy around 90%, with significantly reduced training overhead.

F. Complexity Analysis

To evaluate the feasibility of deploying the proposed method in practical scenarios, we conduct a comparative analysis of the model's number of parameters and inference cost against various baseline approaches. This assessment provides insights into the computational demands and potential deployment challenges associated with each model. The results of this comparison are presented in Table II.

Overall, the inference time per sample for all models is shorter than the data sampling and synchronization intervals.² Notably, due to the inference acceleration capabilities inherent in GPT and BERT models, M²BeamLLM exhibits significantly reduced inference time compared to models like Informer and NLinear. Consequently, the proposed M²BeamLLM demonstrates potential for real-time beam prediction services.

²It is noted that the synchronization interval is 100 ms for DeepSense 6G Scenario 32 (<https://www.deepsense6g.net/data-collection/>).

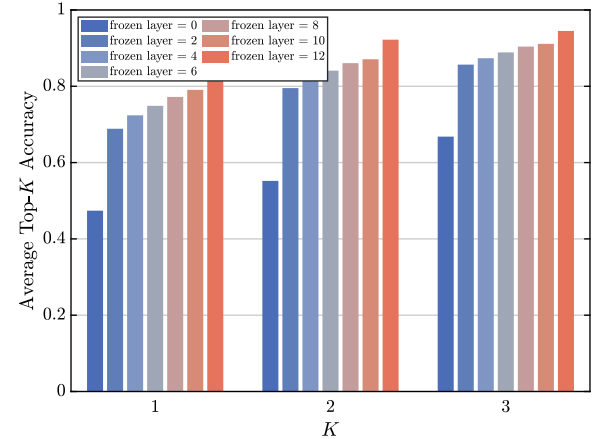


Fig. 19: Comparison of average Top- K accuracy for different numbers of frozen layers.

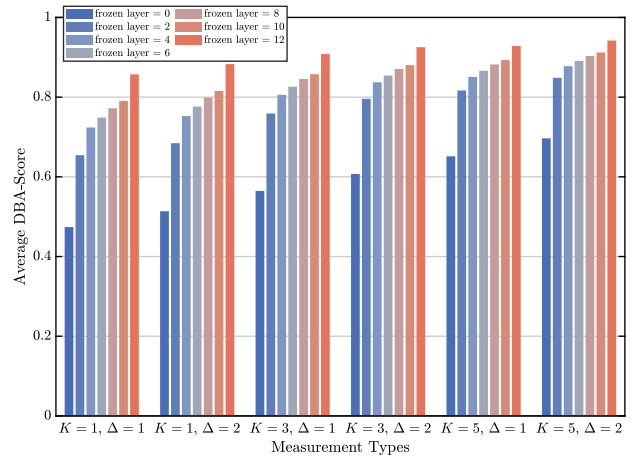


Fig. 20: Comparison of average DBA-score accuracy for different numbers of frozen layers.

V. CONCLUSION

This paper introduced M²BeamLLM, a neural network framework for beam prediction in mmWave mMIMO communication systems. The framework integrates multimodal sensing data, including images, radar, LiDAR, and GPS, and harnesses the powerful inference capabilities of LLMs. M²BeamLLM utilizes multimodal alignment and fusion in conjunction with SFT to improve the accuracy and robustness of beam prediction, significantly outperforming traditional models in both standard and few-shot scenarios. Our findings confirm that the prediction performance of multimodal combinations adheres to the general principle that greater diversity leads to better outcomes. Additionally, we observed that increasing the number of fine-tuning layers enhances prediction performance, albeit at the cost of higher training overhead. Moreover, the inference speed of M²BeamLLM remains comparable to or even faster than baseline models, despite its parameter count being several times higher. This study provided an efficient and intelligent beam prediction solution for V2I mmWave mMIMO communication systems.

TABLE II: Comparison of the network parameters and the interference cost per test sample.

Category	Model	Number of Parameters	Inference Time (10^{-4} s)
Encoders	Vision	11,348,992	/
	Radar	175,254	/
	LiDAR	11,203,072	/
	GPS	6688	/
	Total	22,734,006	/
Prediction	GRU	23 M	1.34
	LSTM	24 M	1.44
	Informer	27 M	4.20
	NLinear	23 M	3.68
	M ² BeamLLM (GPT-2)	147 M	2.55
	M ² BeamLLM (BERT)	132 M	1.84

Nonetheless, there are potential directions for further enhancing this work. A promising avenue involves the design and initialization of a novel large model from the ground up, rather than relying on existing pre-trained LLMs. This foundational model would undergo rigorous pre-training on an extensive dataset, with subsequent fine-tuning adjustments applied during its deployment phase to fully harness its inherent generalization capabilities. Building on this, a more advanced approach would be to design such agent specifically tailored for wireless communication tasks. It would integrate diverse communication and sensing information, such as CSI, images, radar, LiDAR, and GPS data, collected across various times, frequencies, and spatial contexts. Subsequently, at the decoding stage, different decoder modules can be configured to transform the model into an agent framework. This approach significantly enriches the variety of downstream tasks the model can handle—such as beam prediction, channel prediction, blockage prediction, and power control—and allows for direct invocation of different functionalities based on specific task requirements. Moreover, recognizing the practical challenges associated with supervised learning reliant on online labeling, reinforcement learning (RL) presents a viable solution for these tasks [29]. Capitalizing on the formidable inference power of LLMs, this methodology is expected to facilitate the acquisition of underlying regularities within sensing data and beam predictions, entirely bypassing the requirement for explicit labeled data.

REFERENCES

- [1] M. Xiao, S. Mumtaz, Y. Huang, L. Dai, Y. Li, M. Matthaiou, G. K. Karagiannidis, E. Bjornson, K. Yang, C.-L. I, and et al., “Millimeter wave communications for future mobile networks,” *IEEE J. Sel. Areas Commun.*, vol. 35, no. 9, p. 1909–1935, Sep 2017.
- [2] Q. Xue, C. Ji, S. Ma, J. Guo, Y. Xu, Q. Chen, and W. Zhang, “A survey of beam management for mmwave and thz communications towards 6g,” *IEEE Commun. Surveys Tuts.*, vol. 26, no. 3, pp. 1520–1559, 2024.
- [3] M. Alrabeiah and A. Alkhateeb, “Deep learning for mmwave beam and blockage prediction using sub-6 ghz channels,” *IEEE Trans. Commun.*, vol. 68, no. 9, pp. 5504–5518, 2020.
- [4] S. Jiang and A. Alkhateeb, “Computer vision aided beam tracking in A real-world millimeter wave deployment,” in *Proc. IEEE Globecom Workshops (GC Wkshps)*, 2022, pp. 142–147.
- [5] U. Demirhan and A. Alkhateeb, “Radar aided 6G beam prediction: Deep learning algorithms and real-world demonstration,” in *Proc. IEEE Wireless Communications and Networking Conference (WCNC)*, 2022, pp. 2655–2660.
- [6] S. Jiang, G. Charan, and A. Alkhateeb, “LiDAR aided future beam prediction in real-world millimeter wave V2I communications,” *IEEE Wireless Commun. Lett.*, vol. 12, no. 2, pp. 212–216, 2023.
- [7] J. Morais, A. Bchboodi, H. Pezeshki, and A. Alkhateeb, “Position-aided beam prediction in the real world: How useful GPS locations actually are?” in *Proc. IEEE International Conference on Communications (ICC)*, 2023, pp. 1824–1829.
- [8] OpenAI, “GPT-4 technical report,” Accessed Mar. 2023. [Online]. Available: <https://arxiv.org/abs/2303.08774>.
- [9] D. Guo, D. Yang, H. Zhang, J. Song, R. Zhang, R. Xu, Q. Zhu, S. Ma, P. Wang, X. Bi et al., “Deepseek-r1: Incentivizing reasoning capability in LLMs via reinforcement learning,” *arXiv preprint arXiv:2501.12948*, 2025.
- [10] C. Zheng, J. He, G. Cai, Z. Yu, and C. G. Kang, “BeamLLM: Vision-empowered mmWave beam prediction with large language models,” *arXiv preprint arXiv:2503.10432*, 2025.
- [11] L. Cheng, H. Zhang, B. Di, D. Niyato, and L. Song, “Large language models empower multimodal integrated sensing and communication,” *IEEE Commun. Mag.*, vol. 63, no. 5, pp. 190–197, 2025.
- [12] B. Shi, M. Li, M.-M. Zhao, M. Lei, and L. Li, “Multimodal deep learning empowered millimeter-wave beam prediction,” in *Proc. IEEE 99th Vehicular Technology Conference (VTC2024-Spring)*, 2024, pp. 1–6.
- [13] K. Zhang, W. Yu, H. He, S. Song, J. Zhang, and K. B. Letaief, “Multimodal deep learning-empowered beam prediction in future THz ISAC systems,” *arXiv preprint arXiv:2505.02381*, 2025.
- [14] Y. Cui, J. Nie, X. Cao, T. Yu, J. Zou, J. Mu, and X. Jing, “Sensing-assisted high reliable communication: A transformer-based beamforming Approach,” *IEEE J. Sel. Topics Signal Process.*, vol. 18, no. 5, pp. 782–795, 2024.
- [15] C. Zhou, P. Liu, P. Xu, S. Iyer, J. Sun, Y. Mao, X. Ma, A. Efrat, P. Yu, L. Yu, S. Zhang, G. Ghosh, M. Lewis, L. Zettlemoyer, and O. Levy, “LIMA: Less is more for alignment,” in *Proc. Neural Information Processing Systems (NIPS)*, 2023.
- [16] J. Deng, W. Dong, R. Socher, L.-J. Li, K. Li, and L. Fei-Fei, “ImageNet: A large-scale hierarchical image database,” in *Proc. IEEE Conference on Computer Vision and Pattern Recognition (CVPR)*, Jun. 2009, pp. 248–255.
- [17] K. He, X. Zhang, S. Ren, and J. Sun, “Deep residual learning for image recognition,” in *Proc. IEEE Conference on Computer Vision and Pattern Recognition (CVPR)*, Jun. 2016, pp. 770–778.
- [18] Q. Guoqing, “High accuracy range estimation of FMCW level radar based on the phase of the zero-padded FFT,” in *Proc. 7th International Conference on Signal Processing (ICSP)*, vol. 3, 2004, pp. 2078–2081.
- [19] Y. Lecun, L. Bottou, Y. Bengio, and P. Haffner, “Gradient-based learning applied to document recognition,” *Proc. IEEE*, vol. 86, no. 11, pp. 2278–2324, 1998.
- [20] S. Li and H. Tang, “Multimodal alignment and fusion: A survey,” *arXiv preprint arXiv:2411.17040*, 2024.
- [21] A. Radford, J. W. Kim, C. Hallacy, A. Ramesh, G. Goh, S. Agarwal, G. Sastry, A. Askell, P. Mishkin, J. Clark et al., “Learning transferable visual models from natural language supervision,” in *Proc. International Conference on Machine Learning (ICML)*, Jul. 2021, pp. 8748–8763.
- [22] A. Alkhateeb, G. Charan, T. Osman, A. Hredzak, J. Morais, U. Demirhan, and N. Srinivas, “DeepSense 6G: A large-scale real-world multi-modal sensing and communication dataset,” *IEEE Commun. Mag.*, vol. 61, no. 9, pp. 122–128, 2023.
- [23] A. Radford et al., “Language models are unsupervised multitask learners,” *OpenAI blog*, vol. 1, no. 8, p. 9, Feb. 2019.
- [24] K. Cho, B. Van Merriënboer, D. Bahdanau, and Y. Bengio, “On the properties of neural machine translation: encoder-decoder approaches,” *arXiv preprint arXiv:1409.1259*, 2014.
- [25] S. Hochreiter and J. Schmidhuber, “Long short-term memory,” *Neural Computation*, vol. 9, no. 8, pp. 1735–1780, 1997.
- [26] A. Zeng, M. Chen, L. Zhang, and Q. Xu, “Are transformers effective for time series forecasting?” 2023.
- [27] H. Zhou, S. Zhang, J. Peng, S. Zhang, J. Li, H. Xiong, and W. Zhang, “Informer: Beyond efficient transformer for long sequence time-series Forecasting,” in *Proc. AAAI Conference on Artificial Intelligence*, vol. 35, May. 2021, pp. 11 106–11 115.

- [28] D. P. Kingma and J. Ba, "Adam: A method for stochastic optimization," in *Proc. International Conference on Learning Representations (ICLR)*, May. 2015.
- [29] M. Ghassemi, H. Zhang, A. Afana, A. B. Sediq, and M. Erol-Kantarci, "Multi-modal transformer and reinforcement learning-based beam management," *IEEE Netw. Lett.*, vol. 6, no. 4, pp. 222–226, 2024.